

Article

Estimating the Actual Evapotranspiration Using Remote Sensing and SEBAL Model in an Arid Environment of Northwest China

Xietian Chen ¹, Shouchao Yu ¹, Hengjia Zhang ^{1,*}, Fuqiang Li ², Chao Liang ² and Zeyi Wang ²¹ College of Agronomy and Agricultural Engineering, Liaocheng University, Liaocheng 252059, China² College of Water Conservancy and Hydropower Engineering, Gansu Agricultural University, Lanzhou 730070, China

* Correspondence: zhanghj@gsau.edu.cn

Abstract: Evapotranspiration (ET) is an important channel for water transport and energy conversion in land–air systems, and the spatial quantification of actual ET is crucial for water resource management and scheduling in arid areas. Using the Surface Energy Balance Algorithm for Land (SEBAL) model and satellite images, this study determined the actual ET during the growing season of 2020 in the Shiyang River Basin of northwest China and investigated the driving mechanism of ET using a principal component regression. The results showed that the ET obtained using the Penman-Monteith equation exhibited a good correlation with the ET estimated using SEBAL ($R^2 = 0.85$). Additionally, SEBAL overestimated ET to some extent compared to the Moderate-Resolution Imaging Spectroradiometer (MODIS) ET (MOD16) product. The daily ET (ET_d) in the Shiyang River Basin showed a single-peak variation during the growing season, with the maximum value occurring around mid-July. Spatially, the ET gradually increased from northeast to southwest with the variation in the land use/land cover (LULC) type. Among the six LULC types, ET_d was higher for woodland, water body, and grassland, all exceeding 5.0 mm/d; farmland and built-up land had ET_d close to 3.9 mm/d; and barren land had the lowest ET_d of below 2.5 mm/d. Furthermore, the standardized regression coefficients indicated that the Normalized Difference Vegetation Index (NDVI) is the main driving factor influencing ET. Overall, the SEBAL model has the potential to estimate spatially actual ET, and the study results provide a scientific basis for water resource accounting and hydrological analysis in arid areas.

Keywords: evapotranspiration; SEBAL; remote sensing; principal component regression; Shiyang River Basin



Citation: Chen, X.; Yu, S.; Zhang, H.; Li, F.; Liang, C.; Wang, Z. Estimating the Actual Evapotranspiration Using Remote Sensing and SEBAL Model in an Arid Environment of Northwest China. *Water* **2023**, *15*, 1555. <https://doi.org/10.3390/w15081555>

Academic Editor: Junliang Fan

Received: 22 February 2023

Revised: 15 March 2023

Accepted: 13 April 2023

Published: 15 April 2023



Copyright: © 2023 by the authors. Licensee MDPI, Basel, Switzerland. This article is an open access article distributed under the terms and conditions of the Creative Commons Attribution (CC BY) license (<https://creativecommons.org/licenses/by/4.0/>).

1. Introduction

Evapotranspiration (ET) is a critical component of the water cycle and a major process of surface energy exchange, and its intensity is closely related to the soil condition, crop condition, and atmospheric environment [1–3]. In the terrestrial water balance, more than 60% of the rainfall returns to the atmosphere as ET, especially in some dry regions where ET is considerably greater than precipitation, and the water used for ET mainly stems from groundwater and irrigation water [4,5]. Therefore, thoroughly understanding the spatiotemporal distribution of ET in arid regions is important for guiding agricultural irrigation, monitoring drought on farmland, optimizing water allocation, and improving the efficiency of agricultural water use [6,7]. Currently, the ET estimation approaches can be classified into two types. The first type is mainly based on the traditional methods of hydrology and meteorology, including the water balance equation [8], aerodynamic method [9], Priestley and Taylor equation [10], eddy covariance [11], and the Food and Agriculture Organization of the United Nations (FAO) Penman-Monteith (P-M) equation [12]. The other type is mainly based on remote sensing satellite technology modeling approaches, such as

the Simplified Surface Energy Balance Index (S-SEBI) [13], Surface Energy Balance System (SEBS) [14], Two-Source Energy Balance (TSEB) [15], Mapping of Evapotranspiration with Internalized Calibration (METRIC) [16], and Surface Energy Balance Algorithm for Land (SEBAL) [17]. The first type mainly focuses on determining ET at the point scale or in a small region and has difficulty obtaining ET on a wide scale. The second type provides a way to accurately estimate ET for extensive areas through the real-time collection of land surface information during satellite transit. Therefore, more and more studies are applying remote sensing techniques to simulate regional ET based on spatial modeling approaches [18–20].

Among the above-mentioned spatial modeling approaches, the SEBAL model is widely used to simulate the regional ET [21,22]. It was first developed by Bastiaanssen et al. [17] and then improved by Allen et al. [23]. Compared to other models, SEBAL has the advantages of clear physical concepts, low required meteorological data, easy data access, high inversion accuracy, and universal applicability to various climates [24]. Cheng et al. [25] generated a long-time-series daily ET (ET_d) product for China using SEBAL and found that the ET obtained from SEBAL has better precision than the Moderate Resolution Imaging Spectroradiometer (MODIS) ET (MOD16) data. Gao et al. [26] used SEBAL to estimate the actual ET of the Loess Plateau in China and showed that SEBAL has good applicability. Du et al. [27] used SEBAL and MODIS products to invert the ET of the Sanjiang Plain in China. They showed that the deviation between the seasonal ET of SEBAL and the ground observation was within 8.86%, indicating that the ET estimated by SEBAL could help to solve water resource management problems. Kiptala et al. [28] used the multitemporal MODIS and SEBAL to estimate the ET of different land use types during 2008–2010, and they verified the feasibility of SEBAL in estimating ET from various aspects. The above studies basically concluded that the SEBAL algorithm is sufficiently robust for determining the spatial quantities of actual ET.

The Shiyang River Basin, a typical desert–oasis interlacing region, lies in the arid zone of northwest China. The ecological environment of the region is very fragile and has an arid climate, low annual precipitation, and high evaporation; thus, drought and water shortage are the key factors limiting the agricultural and economic development in this region. In recent years, this region has been extensively focused on and has become one of the key management areas of the ecological environment in China. However, relatively few studies have spatially quantified the actual ET in this region. Liu et al. [29] and Tian et al. [30] assessed the distribution characteristics and dynamics of actual ET in the Shiyang River Basin using MOD16 ET products. However, it is important to note that the MOD16 ET products excluded the ET in barren/desert areas from the model calculations and set the ET value to 0. This means that ET could not be estimated for about 60% of the area in the Shiyang River Basin, but the ET in these areas is important for the basin water budget [31]. Therefore, an ET estimation model including barren and sparsely vegetated areas needs to be established to address the limitations of the MOD16 ET products. Furthermore, ET is one of the most challenging components of the water cycle to precisely quantify as it is influenced by multiple factors. Most current studies have estimated the regional ET with little quantitative analysis of its driving factors, especially at the basin scale.

In response to the above issues, this study aims to estimate the actual ET in the Shiyang River Basin of northwest China based on the SEBAL model using remote sensing technology. Moreover, a principal component regression (PCR) is used to explore the relationship between ET and the driving factors. More specifically, this study mainly aims to (1) determine the actual ET_d in the Shiyang River Basin during the 2020 growing season (April–October) using SEBAL, (2) analyze the variation characteristics of actual ET_d under different land use/land cover (LULC) types, and (3) quantitatively characterize the driving factors of ET. The study results will provide a reference for crop water demand research and a plant transpiration characteristics analysis as well as rational allocation of water resources in arid regions.

2. Materials and Methods

2.1. Study Area Description

The Shiyang River Basin is located at $36^{\circ}29'–39^{\circ}27' N$, $101^{\circ}22'–104^{\circ}16' E$, in the eastern part of the Hexi Corridor, China, with a total basin area of approximately $4.06 \times 10^4 \text{ km}^2$ (Figure 1). The basin originates in the northern Qilian Mountains and terminates in the Minqin Oasis, which is a typical oasis-irrigated agricultural area. The area has a temperate continental grassland climate, with perennial drought and little rain, high evaporation, and serious wind and sand hazards. Based on the altitude, rainfall, and evaporation, the Shiyang River Basin can be divided into three climate zones from the south to north: (1) Southern Qilian Mountains alpine semi-arid and semi-humid zone. This region is the water hub of the basin, with an average annual temperature of $2–6^{\circ}C$, elevation between 2000 and 5000 m, annual precipitation of about 300–600 mm, and potential ET of 700–1200 mm; (2) The central plain is a cool and arid zone. In this region, the average annual temperature is higher than that in the southern Qilian Mountains, elevation is 1500–2000 m, annual precipitation is 150–300 mm, and potential ET is 1300–2000 mm; (3) The northern warm arid zone. In this region, the average annual temperature is greater than $8^{\circ}C$, elevation is between 1300 and 1500 m, annual precipitation is less than 150 mm, and potential ET is more than 2000 mm.

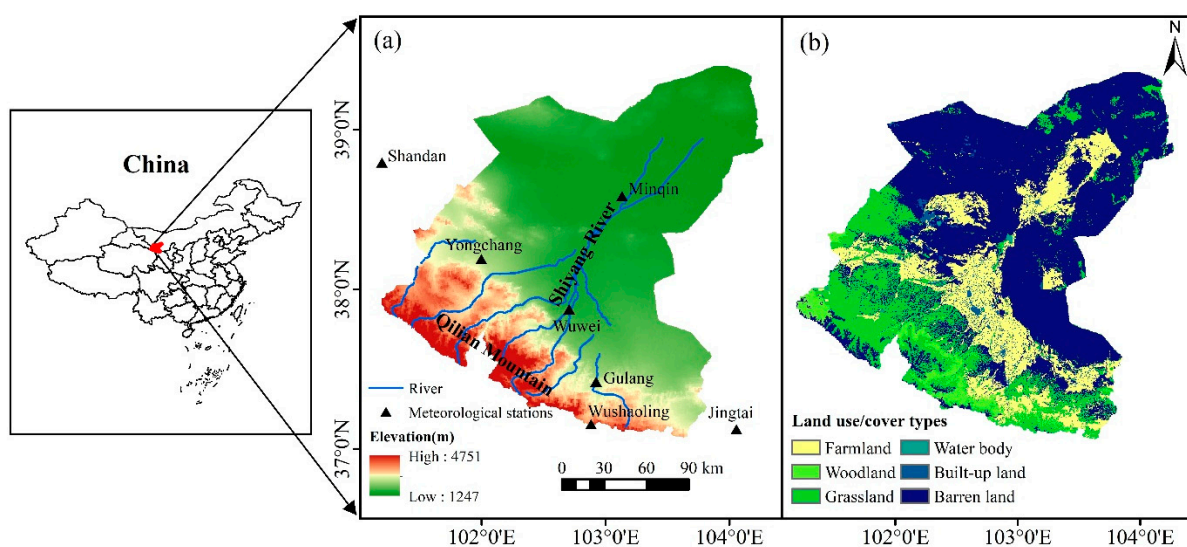


Figure 1. Map of the study area. (a) Location of Shiyang River Basin in northwest China and locations of meteorological stations; (b) land use/land cover map of the study area in 2020.

2.2. Data Collection

2.2.1. MODIS Data

The main input parameters of SEBAL, such as land surface temperature (LST), Normalized Difference Vegetation Index (NDVI), and surface albedo, were obtained from the MODIS products, downloaded from the NASA website (<https://ladsweb.nascom.nasa.gov>, accessed on 6 March 2022), and the detailed image data information is shown in Table 1. Satellite images of the study area from seven periods with low cloudiness from the 2020 growing season were selected, i.e., 22 April (DOY 113), 24 May (DOY 145), 25 June (DOY 177), 11 July (DOY 193), 12 August (DOY 225), 13 September (DOY 257), and 15 October (DOY 289). During the image pre-processing, the raw remote sensing image data were extracted, formatted, and resampled using the MODIS Reprojection Tool, which converted the pixel size to 500 m, the coordinate system to WG-1984, and the data format to the GeoTiff format. Then, the actual ET in the study area was estimated via vector cropping and raster calculation of the processed images using ArcGIS 10.2 (ESRI) software.

Table 1. Detailed information of the MODIS product.

Data Product	Satellite Imagery	Temporal Resolution	Spatial Resolution
MOD11A1/A2	LST/Emissivity	Daily/8 d	1 km
MOD13A1	NDVI	16 d	0.5 km
MOD09A1	Albedo	8 d	0.5 km
MOD16A2	ET _{8d}	8 d	0.5 km

2.2.2. Meteorological Data

Meteorological data, including pan evaporation, temperature, relative humidity, sunshine hours, wind speed, and precipitation, were used as the input data for SEBAL, the P-M equation, and the PCR explanatory variables. Data from meteorological stations in the study area and surrounding areas (Figure 1a) were downloaded from the National Meteorological Information Center of China (<https://Data.cma.cn>, accessed on 13 March 2022). These data were interpolated into a raster of 500 m pixels using an inverse distance weighting method to obtain a spatial distribution that matched the pixels of the MODIS images data.

2.2.3. Other Data

The digital elevation model (DEM) (Figure 1a) and 2020 LULC (Figure 1b) data were obtained from the Center for Resources and Environment, Chinese Academy of Sciences (<http://www.resdc.cn/>, accessed on 12 March 2022). The original resolutions of the DEM and LULC data were 250 and 30 m, respectively. They were resampled to 500 m for consistency with the resolution of the satellite images.

2.3. SEBAL Model

SEBAL is based on the principle of surface energy balance. Its general equation is as follows [17]:

$$LE = R_n - G - H \quad (1)$$

where R_n is the net radiation (W/m^2), G is the soil heat flux (W/m^2), H is the sensible heat flux (W/m^2), and LE is the latent heat flux associated with ET (W/m^2).

2.3.1. Net Radiation Flux (R_n)

R_n is calculated based on the ground radiation flux balance.

$$R_n = (1 - \alpha)R_s \downarrow + R_l \downarrow - R_l \uparrow - (1 - \varepsilon_g)R_l \downarrow \quad (2)$$

where α is the surface albedo, $R_s \downarrow$ is the incoming shortwave radiation (W/m^2), $R_l \downarrow$ is the incoming longwave radiation (W/m^2), $R_l \uparrow$ is the outgoing longwave radiation (W/m^2), and ε_g is the land surface emissivity.

Surface albedo indicates the capacity of the surface to reflect solar radiation. It is calculated as follows [32]:

$$\alpha = \rho_0 + \sum_{i=1}^n \rho_i w_i \quad (3)$$

where n is the number of bands ($n = 7$); ρ_0 is the intercept with a value of -0.0015 ; w_i is a weighting coefficient with values of 0.160, 0.291, 0.243, 0.116, 0.112, 0, and 0.081 [33]; and ρ_i is the reflectance of seven MODIS bands from the MOD09A1 product.

$R_s \downarrow$, $R_l \downarrow$, and $R_l \uparrow$ are calculated as follows [17,34]:

$$R_s \downarrow = G_{sc} \times \cos \theta \times d_r \times \tau_{sw} \quad (4)$$

$$R_l \downarrow = \varepsilon_a \sigma T_a^4 \quad (5)$$

$$R_l \uparrow = \varepsilon_g \sigma T_s^4 \quad (6)$$

where G_{sc} is the solar constant (1367 W/m^2), d_r is the inverse of the square of the relative earth–sun distance, $\cos\theta$ is the cosine of the zenith angle, σ is the Stefan–Boltzmann constant ($5.67 \times 10^{-8} \text{ W/(m}^2 \cdot \text{K}^4)$), τ_{sw} is the atmospheric transmissivity, ε_a is the atmospheric emissivity, and T_a and T_s are the air and land surface temperatures (K), respectively.

2.3.2. Soil Heat Flux (G)

G calculated formulas as follows [35]:

$$G = \frac{T_s - 273.16}{\alpha} (0.0038\alpha + 0.0074\alpha^2) (1 - 0.98NDVI^4) R_n \quad (7)$$

2.3.3. Sensible Heat Flux (H)

H is the parameter characterizing the energy exchange between the surface and atmosphere, which is calculated as follows [23]:

$$H = \frac{\rho_{\text{air}} C_p dT}{r_{\text{ah}}} \quad (8)$$

where ρ_{air} is the air density (kg/m^3), C_p is the air specific heat ($\text{J/(kg}\cdot\text{K)}$), dT is the temperature difference (K), and r_{ah} is the aerodynamic resistance against heat transfer (s/m).

r_{ah} is calculated as follows:

$$r_{\text{ah}} = \frac{\ln\left(\frac{z_1}{z_2}\right)}{kU_f} \quad (9)$$

where k is the von Karman constant (0.41), U_f is the frictional wind speed (m/s) (Equation (10)), and z_1 and z_2 are 0.01 and 2, respectively.

$$U_f = \frac{ku_{200}}{\ln\left(\frac{z_{200}}{z_{0m}}\right)} \quad (10)$$

where u_{200} is the wind speed at height 200 m and z_{0m} is the surface roughness (m), which is calculated as follows [36]:

$$z_{0m} = e^{(5.65NDVI-6.32)} \quad (11)$$

Because dT is difficult to directly calculate, SEBAL assumes a linear relationship between dT and T_s , as shown in Equation (12):

$$dT = aT_s + b \quad (12)$$

To identify the values of a and b , SEBAL needs to be solved by choosing hot and cold pixels. Hot pixels were mainly selected from areas with low vegetation cover and bare ground surface, where LE was negligible and $H \approx R_n - G$. Cold pixels were selected in areas with high vegetation cover as well as adequate and sufficient moisture supply, where H was negligible and $LE \approx R_n - G$. Herein, the specific hot and cold pixel selection was based on LULC, albedo, T_s , and NDVI [37]. It is important to note that the atmospheric stability conditions significantly influence the aerodynamic resistance, and the atmospheric stability conditions should be considered in the H calculation, especially in dry conditions [23]. Therefore, the Monin-Obukhov similarity theory was adopted for iterative calculation to obtain stable values of H and r_{ah} . Detailed computational information regarding the iteration process can be found in Allen et al. [23] and Cheng et al. [25].

2.3.4. Daily ET

LE can be calculated using Equation (1). In this study, the concept of the evaporation fraction (EF) was introduced to extend the instantaneous ET to the daily ET (ET_d). EF refers

to the ratio of LE to the available energy. Many researchers have shown that EF can be considered constant throughout the day [38,39], and EF can be obtained as follows:

$$EF = \frac{LE}{R_n - G} = \frac{R_n - G - H}{R_n - G} \quad (13)$$

Therefore, ET_d can be obtained as follows:

$$ET_d = \frac{86400 \times EF \times (R_{n24} - G_{24})}{(2.501 - 0.002361 \times (T_s - 273.15)) \times 10^6} \quad (14)$$

where R_{n24} is the daily net radiant flux (W/m^2), and G_{24} is the daily soil heat flux (W/m^2).

2.4. Validation Methods

2.4.1. FAO P-M Equation

In this study, the daily reference evapotranspiration (ET_0) was calculated using the P–M equation suggested by the FAO in 1998 [40]. Then, the actual ET_d of the five meteorological stations (Minqin, Wuwei, Wushaoling, Gulang, and Yongchang) in the study area on the remote sensing image acquisition dates was determined by combining the crop coefficients to validate the ET estimated by SEBAL. The calculation equation is as follows:

$$ET_0 = \frac{0.408\Delta(R_n - G) + \gamma \frac{900}{T+273} U_2(e_a - e_d)}{\Delta + \gamma(1 + 0.34U_2)} \quad (15)$$

$$ET = K_c \times ET_0 \quad (16)$$

where γ is the dry wet table constant ($kPa/^\circ C$), T is the daily average temperature ($^\circ C$), U_2 is the wind speed at 2 m height (m/s), Δ is the slope of the saturated vapor pressure curve ($kPa/^\circ C$), and $(e_a - e_d)$ is the water-air pressure difference (kPa). K_c is the crop coefficient.

To obtain the actual ET_d , the K_c value needs to be first determined. The K_c value was calculated using the dual crop coefficient method [41], which divides the crop evapotranspiration into the plant transpiration coefficient and soil evaporation coefficient. The calculation equation is as follows [42]:

$$K_c = K_{cb} + K_e \quad (17)$$

$$K_{cb} = 1.07 \times \left[1 - \left(\frac{NDVI_{max} - NDVI}{NDVI_{max} - NDVI_{min}} \right)^{\frac{0.84}{0.54}} \right] \quad (18)$$

$$K_e = \beta \times (1 - f_c) \quad (19)$$

where K_{cb} is the basic crop coefficient; K_e is the soil evaporation coefficient; $NDVI_{max}$ and $NDVI_{min}$ are the monthly maximum and minimum $NDVI$ values, respectively; f_c is the effective area ratio of the vegetation cover to soil surface; and β is an empirical coefficient, which is assumed to be 0.25 herein based on previous studies [43]. The specific values of K_c in this study are shown in Table 2.

Table 2. K_c values for each meteorological station during the growing season.

Station	April	May	June	July	August	September	October
Minqin	0.53	0.69	1.29	1.29	1.26	0.76	0.37
Wuwei	0.51	0.51	1.28	1.28	1.25	0.66	0.51
Wushaoling	0.38	0.86	1.12	1.13	1.08	0.97	0.48
Gulang	0.34	0.75	0.94	1.27	1.02	0.64	0.41
Yongchang	0.34	0.52	1.00	1.02	1.19	0.71	0.55

2.4.2. Pan Evaporation

Pan evaporation (E_p) can be used to estimate the open water evaporation. In this study, the E_p data from Minqin and Yongchang meteorological stations were used to evaluate the inversion accuracy of SEBAL for water evaporation. Because the pan type of the meteorological stations is E-601 (diameter 62 cm), which cannot be used during the freezing period, only the E_p values from the non-freezing period (May–September) were employed for the evaluation. Furthermore, because of the different evaporation conditions of the pan and open water, a conversion coefficient needed to be introduced to correct for E_p [28]:

$$E_{p(w)} = K_p \times E_p \quad (20)$$

Here, $E_{p(w)}$ is the water evaporation (mm) and K_p is the conversion coefficient. In this study, based on previous related studies [44], the following K_p values were selected: 0.76 (May), 0.75 (June), 0.79 (July), 0.77 (August), and 0.81 (September).

2.4.3. MOD16 ET Product

The MOD16 product is a global ET dataset with a spatial resolution of 500 m; it provides baseline ET flux information for regional and global terrestrial water cycles [45,46]. In this study, SEBAL ET and MOD16 ET were compared to determine whether SEBAL ET is reasonable. However, it is important to note that MOD16 ET was the sum of 8 days within the composite period. Therefore, to align SEBAL ET with MOD16 ET on the time scale, the same percentage variation of ET_0 between the 1-day and 8-day periods was assumed herein. ET_d can be scaled up to the 8-day scale (ET_{8d}) as follows [47]:

$$ET_{8d} = ET_d \times \left(\frac{ET_{0-8d}}{ET_{0-d}} \right) \quad (21)$$

where ET_{0-d} and ET_{0-8d} are the daily reference ET and 8-day reference ET, respectively, which were calculated using the FAO P–M equation.

2.5. Principal Component Regression

The regression model was used to determine the degree of influence of each factor on ET. However, a simple multiple linear regression (MLR) may lead to the distortion of the results in the analysis of the influencing factors because strong multicollinearity usually exists among the variables. Therefore, to eliminate multicollinearity, a PCR was employed in this study for the driving force analysis of ET. The PCR is a regression analysis method that comprises a principal component analysis (PCA) and MLR, which can be implemented in the following two steps.

2.5.1. PCA

The PCA is a common multivariate statistical method that aims to reduce the dimensionality of the variables while maintaining the original information as much as possible. Its calculation process is as follows:

Variable standardization. Because of the different dimensions, the original variables need to be standardized:

$$X^* = (X - \bar{X}) / SD(X) \quad (22)$$

where X^* denotes the standardized variables, X denotes the original variables, \bar{X} denotes the mean value of X , and $SD(X)$ denotes the standard deviation of X .

- (1) Extraction of the principal component (PC). To determine the number of PCs, the cumulative contribution of variance over 85% was used as the selection criterion herein.
- (2) Calculation of the PC score. It is expressed as:

$$\begin{bmatrix} PC_1 \\ PC_2 \\ \vdots \\ PC_i \end{bmatrix} = \begin{bmatrix} C_{11} & C_{12} & \cdots & C_{1j} \\ C_{21} & C_{22} & \cdots & C_{2j} \\ \vdots & \vdots & \vdots & \vdots \\ C_{i1} & C_{i2} & \cdots & C_{ij} \end{bmatrix} \begin{bmatrix} X_1^* \\ X_2^* \\ \vdots \\ X_j^* \end{bmatrix} \tag{23}$$

where C_{ij} denotes the loading coefficients, and X_j^* denotes the standardized variables.

2.5.2. MLR

Using the actual ET as the explained variable and the extracted PCs as the explanatory variables, the MLR equation was developed as follows:

$$y = \sum_{i=1}^n a_i x_i + b \tag{24}$$

where a_i and b are the regression coefficients, which are usually calculated using the least squares method.

2.6. Technical Process

Figure 2 displays the overall framework of this study for estimating the actual ET using SEBAL and remote sensing images, as well as analyzing the ET driving factors using the PCR model.

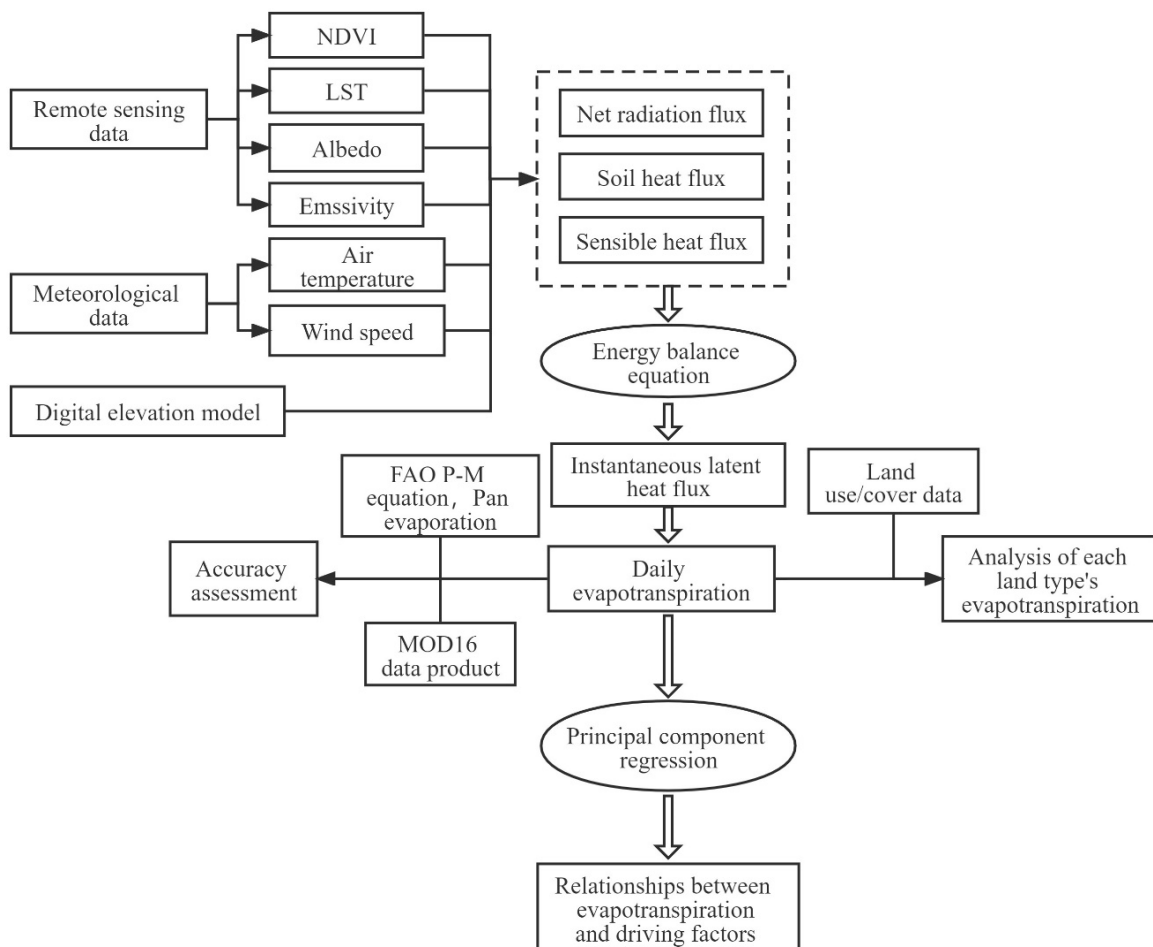


Figure 2. Overall framework diagram.

3. Results

3.1. Accuracy Validation of SEBAL ET

Because no specialized techniques such as ET meters or flux towers have been implemented in the Shiyang River Basin to directly observe ET in situ, the accuracy of SEBAL ET was indirectly assessed using the ET at meteorological stations calculated using the FAO P–M formula (P–M ET) (Figure 3a). The determination coefficient (R^2), root mean square error (RMSE), and mean absolute error (MAE) were selected to quantify the accuracy of SEBAL ET. The results show that SEBAL ET and P–M ET exhibited good correlation with R^2 of 0.85, MAE of 0.76 mm/d, and RMSE of 0.91 mm/d. Furthermore, the water surface evaporation simulated by SEBAL was evaluated using the $E_{p(w)}$ values from the meteorological stations (Figure 3b). The results showed good consistency between SEBAL ET and $E_{p(w)}$, with R^2 of 0.89, MAE of 0.53 mm/d, and RMSE of 0.59 mm/d. The above results denote that the SEBAL results are reliable and valid for the study area.

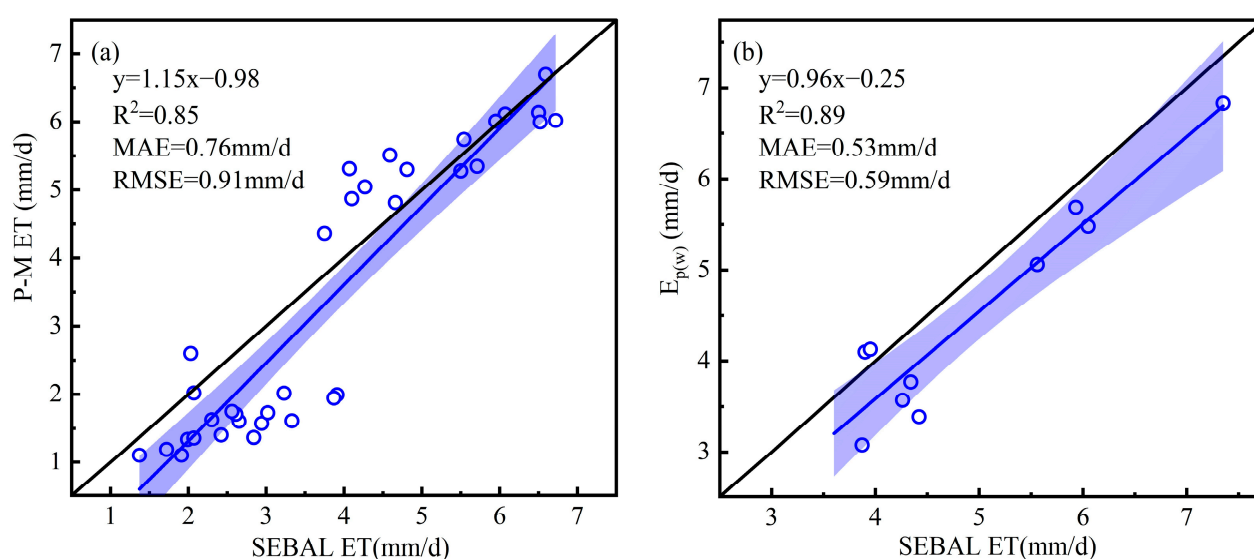


Figure 3. Comparison of SEBAL ET with (a) P-M ET and (b) $E_{p(w)}$.

3.2. Comparison of SEBAL ET and MOD16 ET under Different Land Cover Types

To further validate the assessment performance of SEBAL, SEBAL ET and MOD16 ET were compared. It is important to note that MOD16 ET only provides ET data for vegetation cover surfaces, and ET data for water body, barren land, and built-up land are not available. Therefore, the ET data for the period of DOY 193–DOY 200 (sum of ET for 8 days) in 2020 were selected for comparison because the vegetation was vigorously growing and covering the largest area at this time. Therefore, the MOD16 ET data had fewer missing values. Figure 4 displays the comparison results of SEBAL ET and MOD16 ET for farmland, woodland, and grassland, signifying that the correlation between SEBAL ET and MOD16 ET was the best for grassland with R^2 of 0.52, followed by farmland with R^2 of 0.49, and the worst for woodland with R^2 of 0.41. Compared to MOD16 ET, SEBAL ET was significantly overestimated for woodland and grassland with MAE of 22.79 and 20.57 mm/8d and RMSE of 17.28 and 21.88 mm/8d, respectively. Additionally, the error was smaller for farmland than that for woodland and grassland, with MAE and RMSE of 11.89 and 13.04 mm/8d, respectively. In general, SEBAL ET was significantly higher than MOD16 ET.

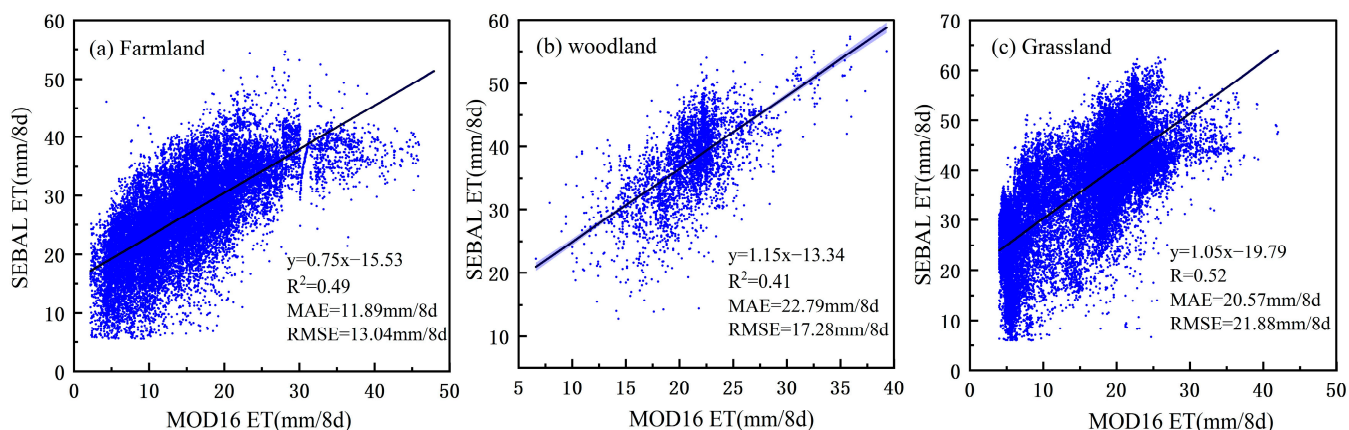


Figure 4. Comparison of SEBAL ET and MOD16 ET for different LULC types in DOY 193–DOY 200 in 2020. (a) Farmland; (b) woodland; and (c) grassland.

3.3. Temporal and Spatial Variation of Actual ET_d

Figure 5a–h display the spatiotemporal variation of the actual ET_d in the Shiyang River Basin simulated by SEBAL. The distribution of ET_d exhibits a unimodal trend during the growing season, with the highest value occurring on DOY 193 in 2020. Specifically, the average ET_d on DOY 113 in 2020 was 2.58 mm/d, and close to 50% of the basin had ET_d of less than 2 mm/d (Figure 5a). The average ET_d on DOY 193 in 2020 increased to 4.77 mm/d, with 62.8% of the area having ET_d of more than 4 mm/d (Figure 5d). The average ET_d on DOY 289 in 2020 decreased to 1.41 mm/d when the number of low-value pixels significantly increased, with nearly three-quarters of the area having an ET_d of less than 2 mm/d (Figure 5g). This trend was observed due to the low temperature, sparse precipitation, and low vegetation coverage in the study area at the initial stage of the growing season, which led to weak transpiration and evaporation. In the middle of the growing season, ET was relatively high due to the gradually increase in temperature, relatively abundant precipitation, increase in snowmelt from the Qilian Mountain, high soil moisture content in farmland supplemented by sufficient irrigation water, and high vegetation cover. However, ET significantly decreased in the late growing season because of the gradual decrease in temperature and precipitation, reduced agricultural irrigation water, slower plant metabolic activity, and crop maturity.

To accurately understand the spatial variation of ET in the study area, the 7-day average ET_d was calculated for each pixel (Figure 5h). The mean ET_d in the study area varied between 0.23 and 7.83 mm/d during the growing season, with a mean ET_d value of 3.45 mm/d for the entire region. From the overall spatial distribution, the spatial divergence of ET from the northeast to southwest was obvious, showing a gradual increase in ET . The reason for this variation is as follows. The southwestern region of the study area is the Qilian Mountain region, which belongs to the upper reaches of the Shiyang River, and the LULC in this region is mainly woodland and high-cover grassland with lush vegetation growth and relatively sufficient precipitation. This region had high ET values. In the middle region of the study area, the main LULC type is farmland, with high water demand for field crops in the middle of the growing season and sufficient water for irrigation. Thus, the ET values in this area were moderate. Additionally, because the northwestern region of the study area comprises the lower reaches of the Shiyang River, the LULC type is dominated by barren/desert land, precipitation is scarce, vegetation is mostly small shrubs and drought-tolerant herbs, and the surface coverage is low. Therefore, the ET values in this area were low.

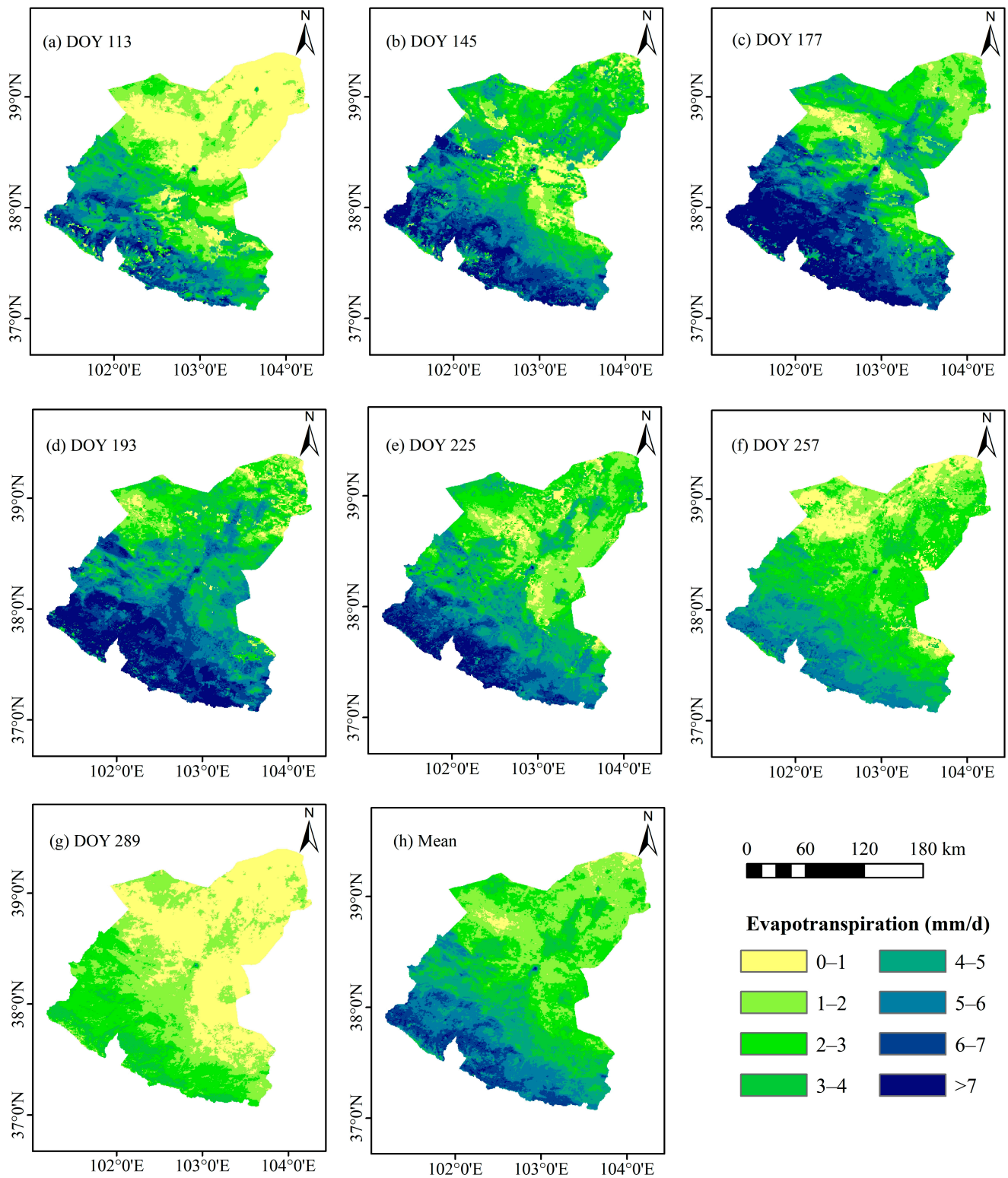


Figure 5. Spatial and temporal distribution of ET_d in the study area in 2020. (a) DOY 113 (22 April); (b) DOY 145 (24 May); (c) DOY 177 (25 June); (d) DOY 193 (11 July); (e) DOY 225 (12 August); (f) DOY 257 (13 September); (g) DOY 289 (15 October); (h) 7-day mean ET.

3.4. Comparison of ET_d in Different LULC Types

The physicochemical properties and underlying surface conditions differed in different LULC types, such as soil texture, soil water content, absorption of radiant energy, and vegetation condition, which are the main factors affecting the spatiotemporal variation of ET. Figure 6a,b display the ET_d variation pattern and the average ET_d performance under different LULC types during the growing season. The figure shows that the ET_d values in the different LULC types first increased and then decreased during the growing season. The ET_d value was the highest for the woodland with a mean value of 6.33 mm/d, followed by the water body and grassland with average ET_d values of 5.17 and 5.05 mm/d, respectively. The ET_d values for farmland and built-up land were close to each other with values of 3.91 and 3.88 mm/d, respectively, while the ET_d value for barren land was the lowest with an average value of 2.45 mm/d. Therefore, the ET_d in different LULC types revealed the following ET performance during the growing season: woodland > water body > grassland > farmland > built-up land > barren land.

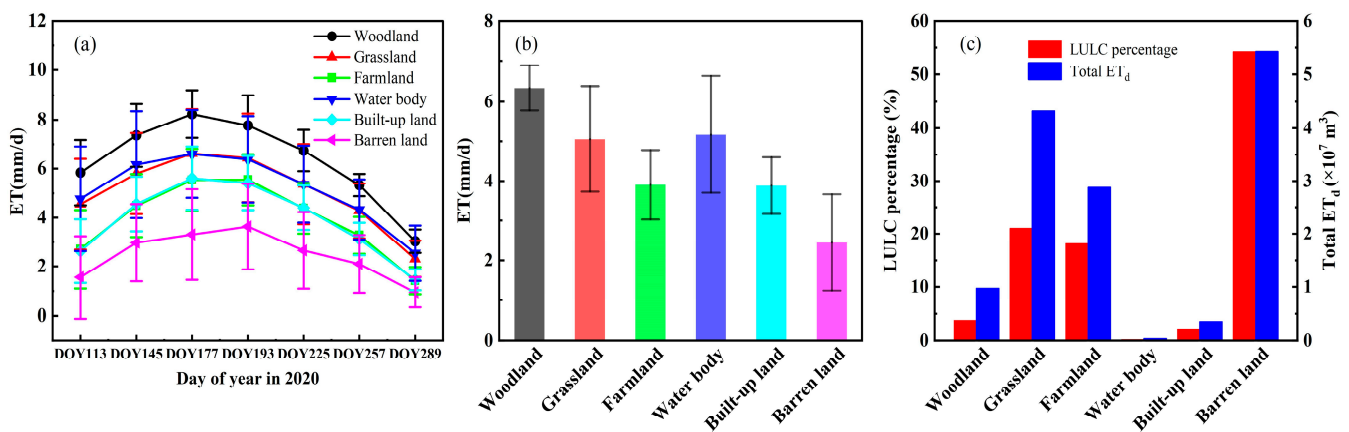


Figure 6. (a) Variation of ET_d in the growing season under different LULC types; (b) average ET_d of different LULC types; (c) total ET_d and area percentage for each LULC type in the study area. Bars indicate standard deviation.

Figure 6c illustrates the total ET_d and area percentage for each LULC type in the study area. As can be seen, barren land had the highest total ET_d value of 5.43×10^7 m³, followed by grassland with 4.32×10^7 m³. Farmland and woodland had total ET_d values of 2.88×10^7 m³ and 9.7×10^6 m³, respectively, while built-up and water body land had the lowest total ET_d values of 3.60×10^6 m³ and 3.71×10^5 m³, respectively. This is closely related to the area of each LULC type in the study area. Barren land and grassland accounted for 54.24% and 21.08% of the total area of the study area, respectively, while water body and built-up land accounted for only 2.45%.

3.5. Analysis of Driving Factors for ET

3.5.1. Correlation Analysis

The level and distribution of ET are usually influenced by various environmental factors. In this study, based on the principles of typicality, dynamics, quantifiability, and availability, eight environmental factors, including NDVI, LST, albedo, DEM, slope (D), precipitation (P), sunshine hours (H), and wind speed (W), were selected from meteorological, vegetation, and topographic factors to determine the effects on the actual ET in the Shiyang River Basin. P denoted the total precipitation during the growing season, while the remaining factors represented the daily averages. The results of the correlation analysis between ET and the eight factors are shown in Figure 7a–h. Significant negative correlations ($p < 0.01$) existed between ET and LST, albedo, and H, with r values of -0.94 , -0.84 , and -0.69 , respectively. Significant positive correlations existed between ET and NDVI, DEM, P, D, and W, with r values of 0.80, 0.86, 0.70, 0.66, and 0.46, respectively. Among the eight

factors, ET was strongly correlated with LST, albedo, NDVI, and DEM, which were the main factors affecting ET.

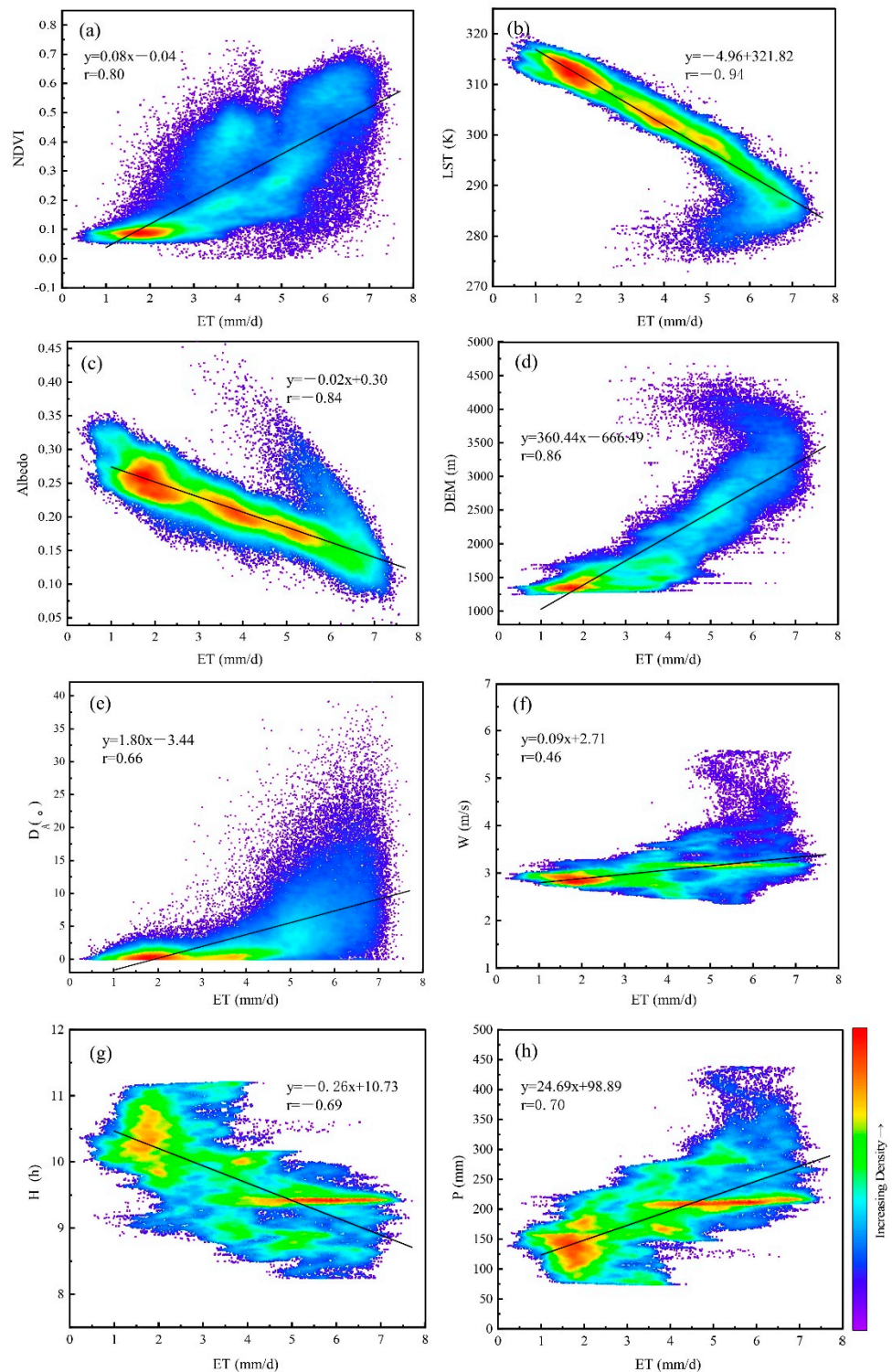


Figure 7. Correlation analysis diagram between ET and (a) NDVI, (b) LST, (c) albedo, (d) DEM, (e) D_A , (f) W, (g) H, and (h) P.

Figure 8 shows the correlation analysis between all the factors. A significant negative correlation existed between NDVI and LST and albedo, with r values of -0.75 for both. LST was significantly negatively correlated with DEM with an r value of -0.92 . DEM was

significantly correlated with P, H, and D, with r values of 0.69, -0.67 , and 0.73 , respectively. P was significantly correlated with H and W, with r values of -0.94 and 0.71 , respectively. The results show that a general correlation exists between the factors, which may lead to some degree of overlap in the information reflected between the factors.

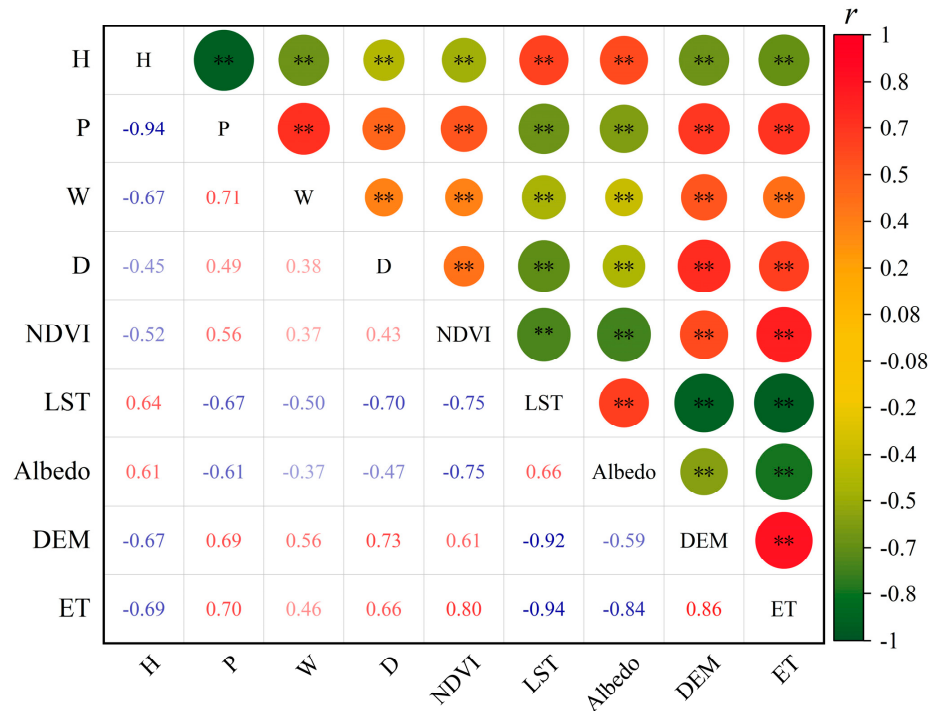


Figure 8. Correlation coefficients between the driving factors. ** represents sig values less than 0.01 ($p < 0.01$).

3.5.2. Principal Component Regression

As shown in Figure 8, generally strong correlations existed among the factors, and direct MLR between ET and the factors may distort the model due to the presence of multicollinearity. Therefore, to eliminate the multicollinearity among the variables, a PCR model was employed to explore the effects of each factor on ET. Three PCs (PC_1 , PC_2 , and PC_3) were extracted based on the principle that the cumulative contribution of variance was greater than 85%, which is shown in Table 3. The eigenvalues of PC_1 , PC_2 , and PC_3 were 5.309, 0.967, and 0.746, respectively, and the cumulative variance contribution of the three PCs was 87.78%, signifying that the selected PCs covered almost all of the information about the indicators.

Based on the calculated PC score coefficient matrix, the equations were listed for PC_1 , PC_2 , and PC_3 using Equation (23):

$$\begin{bmatrix} PC_1 \\ PC_2 \\ PC_3 \end{bmatrix} = \begin{bmatrix} 0.334 & -0.393 & -0.339 & 0.388 & 0.309 & 0.381 & 0.303 & -0.369 \\ -0.345 & 0.271 & 0.243 & -0.156 & -0.324 & 0.383 & 0.554 & -0.408 \\ -0.475 & -0.141 & 0.496 & 0.324 & 0.594 & -0.102 & 0.160 & 0.129 \end{bmatrix} \begin{bmatrix} NDVI^* \\ LST^* \\ Albedo^* \\ DEM^* \\ D^* \\ P^* \\ W^* \\ H^* \end{bmatrix} \tag{25}$$

Table 3. Eigenvalues and variance contribution rates of the PCs.

Principal Components	Initial Eigenvalues and Variance Contribution Rates			Extracted Eigenvalues and Variance Contribution Rates		
	Eigenvalues	Variance Contribution Rates/%	Cumulative Contribution Rates/%	Eigenvalues	Variance Contribution Rates/%	Cumulative Contribution Rates/%
PC ₁	5.309	66.362	66.362	5.309	66.362	66.362
PC ₂	0.967	12.085	78.448	0.967	12.085	78.448
PC ₃	0.746	9.331	87.779	0.746	9.331	87.779
PC ₄	0.379	4.741	92.52			
PC ₅	0.306	3.827	96.346			
PC ₆	0.191	2.390	98.736			
PC ₇	0.052	0.645	99.381			
PC ₈	0.05	0.619	100			

Then, considering the standardized ET as the dependent variable as well as the scores of the three extracted PCs as the explanatory variables, a linear regression model was developed based on Equation (24), which is shown in Equation (26). Equation (26) shows that the standardized ET well-fitted the scores of the three PCs, with R^2 of 0.935:

$$ET^* = 0.399PC_1 - 0.289PC_2 - 0.108PC_3 \quad (R^2 = 0.935) \quad (26)$$

The PC in Equation (24) was substituted into Equation (26) to yield the MLR model between the standardized ET and standardized variables (Equation (27)).

$$ET^* = 0.284NDVI^* - 0.220LST^* - 0.259Albedo^* + 0.165DEM^* + 0.153D^* + 0.052P^* - 0.057W^* - 0.043H^* \quad (27)$$

Because data standardization can eliminate the effect of dimensionality, standardized regression coefficients can be applied to quantitatively characterize the degree of impact of different factors on ET [48]. From Equation (27), the standardized regression coefficients of *NDVI*, *DEM*, *D*, and *P* were positive, indicating that these four factors had positive effects on ET. However, the standardized regression coefficients of *LST*, *A*, *W*, and *H* were negative, showing that these four factors had negative effects on ET. Additionally, the higher the absolute value of the standardized coefficients, the higher the degree of influence. Therefore, the influence degree of the environmental factors on ET was in the order of $NDVI > Albedo > LST > DEM > D > W > P > H$.

4. Discussion

4.1. Accuracy Assessment of ET Estimation Using SEBAL

Remote sensing has become an effective means for estimating ET at a regional or even global scale. However, validating the accuracy of the ET results estimated using remote sensing remains challenging [25,49]. Herein, the SEBAL model was applied using MODIS and meteorological data to determine the actual ET during the 2020 growing season in the Shiyang River Basin. However, due to the complex subsurface conditions and poor ground observation techniques in the Shiyang River Basin, acquiring measured ET data to validate the study results was difficult. Fortunately, previous studies have suggested that the ET calculated using the FAO P-M formula can be applied to indirectly assess the accuracy of ET estimated using remote sensing. Therefore, SEBAL ET and P-M ET were compared. SEBAL ET was well-correlated with P-M ET, with an R^2 of 0.85 and MAE and RMSE of 0.76 and 0.91 mm/d, respectively. Additionally, the $E_{p(w)}$ values observed at the meteorological stations were used to verify the water surface evaporation simulated by SEBAL, and the results showed a good correlation with the R^2 of 0.89 and MAE and RMSE of 0.53 and 0.59 mm/d, respectively. Compared to the results of previous studies (Table 4),

the errors observed herein are acceptable, indicating that the estimation of the actual ET in the study area using SEBAL is feasible.

Table 4. Validation results of SEBAL ET in previous studies.

References	Study Area	Validation Methods	Temporal/ Spatial Resolution	Time	Accuracy Evaluation Results		
					R ²	MAE (mm/d)	RMSE (mm/d)
Li et al. [50]	Agro-pastoral ecotone in northwest China	FAO P-M equation	Daily/1 km	2015	0.76	0.79	0.94
Kong et al. [51]	Ordos Basin in China	FAO P-M equation	Daily/30 m	2015–2016	0.99	0.88	0.97
Ghaderi et al. [52]	Ein Khosh Plain in Iran	FAO P-M equation	Daily/1 km	2015	0.97	0.22	0.47
Rahimzadegan and Janani [53]	A pistachio farm in Semnan Province, Iran	FAO P-M equation	Daily/30 m	2013–2017	0.80	2.09	2.48
Liu et al. [49]	Nukus irrigation area of Amu River Basin	Pan evaporation	Daily/30 m	2019	0.81	/	1.76
Yang et al. [54]	Agro-pastoral ecotone in northwest China	Pan evaporation	Daily/30 m	2016–2017	0.81	/	0.90

Additionally, SEBAL ET was compared with MOD16 ET for different LULC types to determine whether SEBAL ET had a better performance. The results showed that SEBAL ET was significantly higher than MOD16 ET, especially in the woodland and grassland, with the MAE of both exceeding 20 mm/8 d. This is consistent with the results by Cheng et al. [25], who determined that in 84% of the areas in China, SEBAL ET was higher than MOD16 ET, and in 14% of the areas, the difference was more than two times. Autovino et al. [55] and Srivastava et al. [56] found that the MOD16 product generally underestimated ET compared to the ET observed on the ground. In this study, the reasons for this large error can be summarized in terms of two aspects: (1) the initial MOD16 algorithm significantly underestimated the global vegetation surface ET [57], and then, Mu et al. [58] enhanced the accuracy of the estimated ET by improving the MOD16 algorithm. However, the improved MOD16 algorithm still makes some inherent assumptions, such as the stomatal closure at night, which could lead to bias in plant nocturnal transpiration and thus cause underestimation of ET_d [45]. (2) Several assumptions in the estimation of H using SEBAL could cause an overestimation of ET if not applied correctly, especially in arid regions and/or sparse canopies [59]. To estimate H, the SEBAL algorithm introduced a temperature gradient dependent on two extreme pixels (cold and hot pixels), and the user's subjective decision in selecting these hot and cold pixel points (although there were many suggestions) could introduce uncertainty into the modeling results. In addition to H, the calculation of R_n and G through some empirical formulae could result in uncertainties in ET estimates [60,61].

4.2. Analysis of the ET_d with Different LULC Types

During the growing season, the ET_d distribution in the Shiyang River Basin showed a unimodal variation, with the maximum value occurring in mid-July. The same conclusion was reported by Liu et al. [29] using the MOD16 ET product, who suggested that the distribution trend of ET_d was related to changes in irrigation water, temperature, precipitation, and vegetation within the Shiyang River Basin. Spatially, ET in the study area decreased from the southwest to northeast. Although the southwest region of the basin has a higher altitude and lower temperature, there are more woodlands and high cover grasslands with high precipitation and a sufficient water supply. The northeastern region of the basin is at a lower altitude, but it is mostly sparse grassland and barren land with insufficient water supply. Therefore, in the study area, the ET in the northeast is much lower than that in the southwest.

The results also showed that the ET_d values of different LULC types had the order of woodland > water body > grassland > farmland > built-up land > barren land. This is similar to the findings of Kiptala et al. [28], who suggested that the ET values were the highest in the water body and woodland, followed by irrigated farmland, while grassland and barren land had the lowest ET values. Woodland has the dual functions of water conservation and transpiration, which can provide a good water supply for ET; therefore, its ET is relatively high. However, the percentage of woodland in the study area was less than 4%, while barren and grassland accounted for more than 75% of the study area. Thus, the total ET_d of the barren land and grassland was much higher than that of the woodland. Moreover, farmland accounted for about 18% of the study area and had a high ET; therefore, farmland is the third highest LULC type in terms of total ET_d . The built-up land and water body only accounted for approximately 2.5% of the study area, and hence, both had a considerably low total ET_d .

4.3. Impact of Environmental Factors on ET

A correlation analysis was performed to investigate the relationship between environmental factors and ET. The results showed that ET was strongly correlated with LST, albedo, NDVI, and DEM, with r values greater than 0.8. Among them, ET was positively correlated with NDVI and DEM and negatively correlated with LST and albedo, which is consistent with the findings of previous studies. Using SEBAL, Li et al. [50] found that ET and NDVI were positively correlated ($r = 0.53$) and ET and LST ($r = -0.86$) and albedo ($r = -0.57$) were negatively correlated in northwest China. Yang et al. [62] revealed that ET was positively correlated with NDVI and negatively correlated with LST, and the r value between ET and LST was higher than that between ET and NDVI. Additionally, a PCR model was introduced herein to quantitatively characterize the degree of impact of each environmental factor on ET, and the results showed that there was good fitness between ET and the environmental factors, with an adjusted R^2 of 0.935. The standardized regression coefficients showed that the influence degree of environmental factors on ET in descending order was NDVI, albedo, LST, DEM, D, W, P, and H. Lin et al. [63] used a ridge regression model to investigate the driving forces of ET in the Sanjiang Plain of China and showed that precipitation was the primary factor impacting ET in this region, followed by NDVI, which is somewhat different from the findings of this study. This is because the Sanjiang Plain belongs to the humid zone, where precipitation is the main source of ET. However, precipitation is scarce in the Shiyang River Basin and the main source of ET is irrigation or groundwater, which leads to a reduced effect of precipitation on ET. Additionally, Yang et al. [64] explored the influencing factors of ET in the Haihe River Basin using the structural equation model. They showed that the direct effect of meteorological factors on ET was not significant and that it tended to indirectly affect ET by influencing vegetation changes, providing a reasonable explanation for the fact that the degree of influence of the meteorological factors (P, W, and H) on ET was less than that of NDVI on ET in this study.

4.4. Limitations and Outlook

In this study, remote sensing images (e.g., NDVI, LST, and surface albedo) were the main input data of SEBAL. However, previous studies found that the accuracy of the original MODIS data is uncertain to some extent, which leads to errors between the ET estimated by SEBAL and the actual ET in the study area [25,65]. The low resolution of remote sensing images and improper parameter calculation methods in the algorithm also affect the simulation accuracy of SEBAL. Future studies should use high-resolution images as model inputs, while continuously improving the SEBAL algorithm, for example, calibrating the empirical equation of daily mean net radiation to improve ET_d estimates, and developing automatic identification procedures for cold and hot pixels to eliminate user subjectivity. Additionally, the present study area lacks in situ flux data to validate the

estimates of ET and other fluxes. Therefore, the estimation results should be validated by multiple in situ flux data as far as possible in the future.

5. Conclusions

Using SEBAL, the actual ET during the 2020 growing season in the Shiyang River Basin of northwest China was estimated. Subsequently, the spatiotemporal distribution and dynamics of ET for different LULC types were investigated and the driving forces of ET were explored. The results showed that SEBAL ET exhibited good correlation with P-M ET ($R^2 = 0.85$) and $E_{p(w)}$ ($R^2 = 0.89$), indicating that SEBAL has the potential to estimate the actual ET in the Shiyang River Basin. Moreover, SEBAL significantly overestimated ET compared to MOD16, which could be caused by the underestimation of ET from the MOD16 algorithm and the uncertainty of SEBAL itself. The ET in the study area exhibited a single-peak variation during the growing season, with the peak occurring in mid-July. Spatially, the ET values were higher in the woodland and grassland in the southwestern part of the study area and lower in the sparse grasslands and desert areas in the northeastern part. The ET values in different LULC types were in the order of woodland > water body > grassland > cropland > building land > barren land. Additionally, the correlation analysis showed that ET was significantly correlated with LST, DEM, albedo, and NDVI, with r values exceeding 0.8. The PCR concluded that NDVI was the major driving factor impacting ET, and the direct effect of meteorological factors (precipitation, wind speed, and sunshine hours) on ET was not significant. Furthermore, it is important to note that there was still uncertainty in the estimation of the surface energy components using SEBAL as well as difficulty in validating the accuracy of the estimation results. Therefore, future studies will concentrate on the improvement of the SEBAL algorithm and the multi-scale and multi-method accuracy validation of the simulation results.

Author Contributions: Data curation, X.C., F.L. and C.L.; formal analysis, X.C. and Z.W.; funding acquisition, H.Z.; writing—original draft, X.C.; supervision, H.Z. and S.Y.; writing—review and editing, X.C. and H.Z. All authors have read and agreed to the published version of the manuscript.

Funding: This work was supported by the National Natural Science Foundation of China (No. 52269008), the Industrial Support Plan Project of Gansu Provincial Department of Education (No. 2022CYZC-51), the Key Research and Planning Projects of Gansu Province (No. 18YF1NA073), and the National Natural Science Foundation of China (No. 51669001).

Institutional Review Board Statement: Not applicable.

Informed Consent Statement: Not applicable.

Data Availability Statement: The datasets used and/or analyzed during the current study are available from the corresponding author upon reasonable request and the approval of the data owner.

Conflicts of Interest: The authors declare no conflict of interest.

References

1. Xiong, Y.J.; Zhao, S.H.; Tian, F.; Qiu, G.Y. An evapotranspiration product for arid regions based on the three-temperature model and thermal remote sensing. *J. Hydrol.* **2015**, *530*, 392–404. [[CrossRef](#)]
2. Sun, S.K.; Li, C.; Wang, Y.B.; Zhao, X.N.; Wu, P.T. Evaluation of the mechanisms and performances of major satellite-based evapotranspiration models in Northwest China. *Agric. For. Meteorol.* **2020**, *291*, 15. [[CrossRef](#)]
3. Cui, Y.K.; Jia, L.; Fan, W.J. Estimation of actual evapotranspiration and its components in an irrigated area by integrating the Shuttleworth-Wallace and surface temperature-vegetation index schemes using the particle swarm optimization algorithm. *Agric. For. Meteorol.* **2021**, *307*, 15. [[CrossRef](#)]
4. Kite, G. Using a basin-scale hydrological model to estimate crop transpiration and soil evaporation. *J. Hydrol.* **2000**, *229*, 59–69. [[CrossRef](#)]
5. Gao, J.Q.; Qiao, M.; Qiu, X.F.; Zeng, Y.; Hua, H.H.; Ye, X.Z.; Adamu, M. Estimation of Actual Evapotranspiration Distribution in the Huaihe River Upstream Basin Based on the Generalized Complementary Principle. *Adv. Meteorol.* **2018**, *2018*, 9. [[CrossRef](#)]
6. Jiang, X.W.; Sun, Z.C.; Zhao, K.Y.; Shi, F.S.; Wan, L.; Wang, X.S.; Shi, Z.M. A method for simultaneous estimation of groundwater evapotranspiration and inflow rates in the discharge area using seasonal water table fluctuations. *J. Hydrol.* **2017**, *548*, 498–507. [[CrossRef](#)]

7. Rwasoka, D.T.; Gumindoga, W.; Gwenzi, J. Estimation of actual evapotranspiration using the Surface Energy Balance System (SEBS) algorithm in the Upper Manyame catchment in Zimbabwe. *Phys. Chem. Earth* **2011**, *36*, 736–746. [[CrossRef](#)]
8. Rana, G.; Katerji, N. Measurement and estimation of actual evapotranspiration in the field under Mediterranean climate: A review. *Eur. J. Agron.* **2000**, *13*, 125–153. [[CrossRef](#)]
9. Thornthwaite, C.; Holzman, B. The determination of evaporation from land and water surfaces. *Mon. Weather Rev.* **1939**, *67*, 4–11. [[CrossRef](#)]
10. Priestley, C.H.B.; Taylor, R.J. On the assessment of surface heat flux and evaporation using large-scale parameters. *Mon. Weather Rev.* **1972**, *100*, 81–92. [[CrossRef](#)]
11. Montgomery, R. Vertical eddy flux of heat in the atmosphere. *J. Atmos. Sci.* **1948**, *5*, 265–274. [[CrossRef](#)]
12. Allen, R.G.; Pereira, L.S.; Raes, D.; Smith, M. Crop evapotranspiration—Guidelines for computing crop water requirements—FAO Irrigation and drainage paper 56. *Fao. Rome* **1998**, *300*, D05109.
13. Roerink, G.; Su, Z.; Menenti, M. S-SEBI: A simple remote sensing algorithm to estimate the surface energy balance. *Phys. Chem. Earth* **2000**, *25*, 147–157. [[CrossRef](#)]
14. Su, Z. The Surface Energy Balance System (SEBS) for estimation of turbulent heat fluxes. *Hydrol. Earth Syst. Sci.* **2002**, *6*, 85–100. [[CrossRef](#)]
15. Song, L.S.; Liu, S.M.; Kustas, W.P.; Zhou, J.; Xu, Z.W.; Xia, T.; Li, M.S. Application of remote sensing-based two-source energy balance model for mapping field surface fluxes with composite and component surface temperatures. *Agric. For. Meteorol.* **2016**, *230*, 8–19. [[CrossRef](#)]
16. Allen, R.G.; Tasumi, M.; Trezza, R. Satellite-based energy balance for mapping evapotranspiration with internalized calibration (METRIC)—Model. *J. Irrig. Drain. Eng.* **2007**, *133*, 380–394. [[CrossRef](#)]
17. Bastiaanssen, W.G.; Menenti, M.; Feddes, R.; Holtslag, A. A remote sensing surface energy balance algorithm for land (SEBAL). 1. Formulation. *J. Hydrol.* **1998**, *212*, 198–212. [[CrossRef](#)]
18. Elnmer, A.; Khadr, M.; Kanae, S.; Tawfik, A. Mapping daily and seasonally evapotranspiration using remote sensing techniques over the Nile delta. *Agric. Water Manag.* **2019**, *213*, 682–692. [[CrossRef](#)]
19. Wagle, P.; Gowda, P.H.; Northup, B.K. Dynamics of evapotranspiration over a non-irrigated alfalfa field in the Southern Great Plains of the United States. *Agric. Water Manag.* **2019**, *223*, 105727. [[CrossRef](#)]
20. Chen, J.M.; Chen, X.; Ju, W.; Geng, X. Distributed hydrological model for mapping evapotranspiration using remote sensing inputs. *J. Hydrol.* **2005**, *305*, 15–39. [[CrossRef](#)]
21. Usman, M.; Liedl, R.; Awan, U.K. Spatio-temporal estimation of consumptive water use for assessment of irrigation system performance and management of water resources in irrigated Indus Basin, Pakistan. *J. Hydrol.* **2015**, *525*, 26–41. [[CrossRef](#)]
22. Teixeira, A.d.C.; Bastiaanssen, W.G.; Ahmad, M.; Bos, M. Reviewing SEBAL input parameters for assessing evapotranspiration and water productivity for the Low-Middle Sao Francisco River basin, Brazil: Part A: Calibration and validation. *Agric. For. Meteorol.* **2009**, *149*, 462–476. [[CrossRef](#)]
23. Allen, R.; Tasumi, M.; Trezza, R.; Waters, R.; Bastiaanssen, W. *SEBAL (Surface Energy Balance Algorithms for Land)—Advanced Training and Users Manual—Idaho Implementation (Version 1.0)*; The Idaho Department of Water Resources: Boise, ID, USA, 2002.
24. Yang, Y.M.; Zhou, X.Y.; Yang, Y.H.; Bi, S.J.; Yang, X.H.; Liu, D.L. Evaluating water-saving efficiency of plastic mulching in Northwest China using remote sensing and SEBAL. *Agric. Water Manag.* **2018**, *209*, 240–248. [[CrossRef](#)]
25. Cheng, M.H.; Jiao, X.Y.; Li, B.B.; Yu, X.; Shao, M.C.; Jin, X.L. Long time series of daily evapotranspiration in China based on the SEBAL model and multisource images and validation. *Earth Syst. Sci. Data* **2021**, *13*, 3995–4017. [[CrossRef](#)]
26. Gao, X.R.; Sun, M.; Luan, Q.H.; Zhao, X.N.; Wang, J.C.; He, G.H.; Zhao, Y. The spatial and temporal evolution of the actual evapotranspiration based on the remote sensing method in the Loess Plateau. *Sci. Total Environ.* **2020**, *708*, 11. [[CrossRef](#)]
27. Du, J.; Song, K.; Wang, Z.; Zhang, B.; Liu, D. Evapotranspiration estimation based on MODIS products and surface energy balance algorithms for land (SEBAL) model in Sanjiang Plain, Northeast China. *Chin. Geogr. Sci.* **2013**, *23*, 73–91. [[CrossRef](#)]
28. Kiptala, J.K.; Mohamed, Y.; Mul, M.L.; Van der Zaag, P. Mapping evapotranspiration trends using MODIS and SEBAL model in a data scarce and heterogeneous landscape in Eastern Africa. *Water Resour. Res.* **2013**, *49*, 8495–8510. [[CrossRef](#)]
29. Liu, J.F.; Xiong, Y.J.; Tian, J.L.; Tan, Z.H. Spatiotemporal Changes in Evapotranspiration from an Overexploited Water Resources Basin in Arid Northern China and Their Implications for Ecosystem Management. *Sustainability* **2019**, *11*, 445. [[CrossRef](#)]
30. Tian, F.; Zhang, Y. Spatiotemporal patterns of evapotranspiration, gross primary productivity, and water use efficiency of cropland in agroecosystems and their relation to the water-saving project in the Shiyang River Basin of Northwestern China. *Comput. Electron. Agric.* **2020**, *172*, 16. [[CrossRef](#)]
31. Li, Z.L.; Tang, R.; Wan, Z.M.; Bi, Y.Y.; Zhou, C.H.; Tang, B.H.; Yan, G.J.; Zhang, X.Y. A review of current methodologies for regional evapotranspiration estimation from remotely sensed data. *Sensors* **2009**, *9*, 3801–3853. [[CrossRef](#)]
32. Starks, P.J.; Norman, J.M.; Blad, B.L.; Walter-Shea, E.A.; Walthall, C.L. Estimation of shortwave hemispherical reflectance (albedo) from bidirectionally reflected radiance data. *Remote Sens. Environ.* **1991**, *38*, 123–134. [[CrossRef](#)]
33. Liang, S. Narrowband to broadband conversions of land surface albedo I: Algorithms. *Remote Sens. Environ.* **2001**, *76*, 213–238. [[CrossRef](#)]
34. Allen, R.G.; Tasumi, M.; Morse, A. Satellite-based evapotranspiration by METRIC and Landsat for western states water management. In Proceedings of the US Bureau of Reclamation Evapotranspiration Workshop, Fort Collins, CO, USA, 8–10 February 2005; pp. 8–10.

35. Bastiaanssen, W.G. SEBAL-based sensible and latent heat fluxes in the irrigated Gediz Basin, Turkey. *J. Hydrol.* **2000**, *229*, 87–100. [[CrossRef](#)]
36. Moran, M.S.; Jackson, R.D. Assessing the spatial distribution of evapotranspiration using remotely sensed inputs. *J. Environ. Qual.* **1991**, *20*, 725–737. [[CrossRef](#)]
37. Li, X.L.; Xu, X.F.; Wang, X.J.; Xu, S.Y.; Tian, W.; Tian, J.; He, C.S. Assessing the Effects of Spatial Scales on Regional Evapotranspiration Estimation by the SEBAL Model and Multiple Satellite Datasets: A Case Study in the Agro-Pastoral Ecotone, Northwestern China. *Remote Sens.* **2021**, *13*, 1524. [[CrossRef](#)]
38. Shuttleworth, W.; Gurney, R.; Hsu, A.; Ormsby, J. FIFE: The variation in energy partition at surface flux sites. *IAHS Publ.* **1989**, *186*, 523–534.
39. Crago, R.D. Conservation and variability of the evaporative fraction during the daytime. *J. Hydrol.* **1996**, *180*, 173–194. [[CrossRef](#)]
40. Allen, R.G. Crop Evapotranspiration—Guideline for computing crop water requirements. *Irrig. Drain* **1998**, *56*, 300.
41. Wright, J.L. New evapotranspiration crop coefficients. *J. Irrig. Drain. Div.* **1982**, *108*, 57–74. [[CrossRef](#)]
42. Deng, H.J.; Lu, Y.J.; Wang, Y.Y.; Chen, X.W.; Liu, Q. Assessment of actual evapotranspiration in the Minjiang River Basin Based on the GLDAS-Noah model. *Sci. Geogr. Sin.* **2022**, *42*, 548–556. [[CrossRef](#)]
43. Abid, N.; Bargaoui, Z.; Mannaerts, C.M. Remote-sensing estimation of the water stress coefficient and comparison with drought evidence. *Int. J. Remote Sens.* **2018**, *39*, 4616–4639. [[CrossRef](#)]
44. Tang, K.; Jiang, H.B.; He, X.L.; Ji, L.; Zhang, S.B. Research on characteristics and reduction technology of water surface evaporation in arid area. *J. Water Res. Eng.* **2014**, *6*, 68–71. [[CrossRef](#)]
45. Kim, H.W.; Hwang, K.; Mu, Q.; Lee, S.O.; Choi, M. Validation of MODIS 16 Global Terrestrial Evapotranspiration Products in Various Climates and Land Cover Types in Asia. *KSCE J. Civ. Eng.* **2012**, *16*, 229–238. [[CrossRef](#)]
46. He, M.Z.; Kimball, J.S.; Yi, Y.H.; Running, S.W.; Guan, K.Y.; Moreno, A.; Wu, X.C.; Maneta, M. Satellite data-driven modeling of field scale evapotranspiration in croplands using the MOD16 algorithm framework. *Remote Sens. Environ.* **2019**, *230*, 13. [[CrossRef](#)]
47. Gobbo, S.; Lo Presti, S.; Martello, M.; Panunzi, L.; Berti, A.; Morari, F. Integrating SEBAL with in-Field Crop Water Status Measurement for Precision Irrigation Applications—A Case Study. *Remote Sens.* **2019**, *11*, 2069. [[CrossRef](#)]
48. Chen, M.T.; Luo, Y.F.; Shen, Y.Y.; Han, Z.Z.; Cui, Y.L. Driving force analysis of irrigation water consumption using principal component regression analysis. *Agric. Water Manag.* **2020**, *234*, 14. [[CrossRef](#)]
49. Liu, Z.B.; Huang, Y.; Liu, T.; Li, J.L.; Xing, W.; Akmalov, S.; Peng, J.B.; Pan, X.H.; Guo, C.Y.; Duan, Y.C. Water Balance Analysis Based on a Quantitative Evapotranspiration Inversion in the Nukus Irrigation Area, Lower Amu River Basin. *Remote Sens.* **2020**, *12*, 2317. [[CrossRef](#)]
50. Li, X.L.; Yang, L.X.; Xu, X.F.; Tian, W.; He, C.S. Analysis of evapotranspiration pattern by SEBAL model during the growing season in the agro-pastoral ecotone in Northwest China. *Acta Ecol. Sin.* **2020**, *40*, 2175–2185.
51. Kong, J.L.; Hu, Y.X.; Yang, L.Y.; Shan, Z.B.; Wang, Y.T. Estimation of evapotranspiration for the blown-sand region in the Ordos basin based on the SEBAL model. *Int. J. Remote Sens.* **2019**, *40*, 1945–1965. [[CrossRef](#)]
52. Ghaderi, A.; Dasineh, M.; Shokri, M.; Abraham, J. Estimation of actual evapotranspiration using the remote sensing method and SEBAL algorithm: A case study in Ein Khosh Plain, Iran. *Hydrology* **2020**, *7*, 36. [[CrossRef](#)]
53. Rahimzadegan, M.; Janani, A. Estimating evapotranspiration of pistachio crop based on SEBAL algorithm using Landsat 8 satellite imagery. *Agric. Water Manag.* **2019**, *217*, 383–390. [[CrossRef](#)]
54. Yang, L.Y.; Li, J.F.; Sun, Z.H.; Liu, J.B.; Yang, Y.Y.; Li, T. Daily actual evapotranspiration estimation of different land use types based on SEBAL model in the agro-pastoral ecotone of northwest China. *PLoS ONE* **2022**, *17*, e0265138. [[CrossRef](#)]
55. Autovino, D.; Minacapilli, M.; Provenzano, G. Modelling bulk surface resistance by MODIS data and assessment of MOD16A2 evapotranspiration product in an irrigation district of Southern Italy. *Agric. Water Manag.* **2016**, *167*, 86–94. [[CrossRef](#)]
56. Srivastava, A.; Sahoo, B.; Raghuvanshi, N.S.; Singh, R. Evaluation of Variable-Infiltration Capacity Model and MODIS-Terra Satellite-Derived Grid-Scale Evapotranspiration Estimates in a River Basin with Tropical Monsoon-Type Climatology. *J. Irrig. Drain. Eng.* **2017**, *143*, 16. [[CrossRef](#)]
57. Mu, Q.; Heinsch, F.A.; Zhao, M.; Running, S. Development of a global evapotranspiration algorithm based on MODIS and global meteorology data. *Remote Sens. Environ.* **2007**, *111*, 519–536. [[CrossRef](#)]
58. Mu, Q.; Zhao, M.; Running, S.W. Improvements to a MODIS global terrestrial evapotranspiration algorithm. *Remote Sens. Environ.* **2011**, *115*, 1781–1800. [[CrossRef](#)]
59. Zheng, C.; Wang, Q.; Li, P. Coupling SEBAL with a new radiation module and MODIS products for better estimation of evapotranspiration. *Hydrol. Sci. J.* **2016**, *61*, 1535–1547. [[CrossRef](#)]
60. Song, R.; Muller, J.-P.; Kharbouche, S.; Yin, F.; Woodgate, W.; Kitchen, M.; Roland, M.; Arriga, N.; Meyer, W.; Koerber, G.; et al. Validation of Space-Based Albedo Products from Upscaled Tower-Based Measurements Over Heterogeneous and Homogeneous Landscapes. *Remote Sens.* **2020**, *12*, 833. [[CrossRef](#)]
61. Li, Y.; Huang, C.L.; Hou, J.L.; Gu, J.; Zhu, G.F.; Li, X. Mapping daily evapotranspiration based on spatiotemporal fusion of ASTER and MODIS images over irrigated agricultural areas in the Heihe River Basin, Northwest China. *Agric. For. Meteorol.* **2017**, *244*, 82–97. [[CrossRef](#)]
62. Yang, J.Y.; Mei, X.R.; Huo, Z.G.; Yan, C.R.; Ju, H.; Zhao, F.H.; Liu, Q. Water consumption in summer maize and winter wheat cropping system based on SEBAL model in Huang-Huai-Hai Plain, China. *J. Integr. Agric.* **2015**, *14*, 2065–2076. [[CrossRef](#)]

63. Lin, N.; Jiang, R.Z.; Liu, Q.; Guo, X.D.; Yang, H.; CHEN, S. Spatiotemporal characteristics and driving factors of surface evapotranspiration in Sanjiang Plain in recent 20 years. *Geol. China* **2021**, *48*, 1392–1407.
64. Yang, W.J.; Zhao, J.S.; Zhao, Y.; Wang, Q.M. Factors affecting evapotranspiration analyzed based on a structural equation model. *J. Tsinghua Univ.* **2022**, *62*, 581–588. [[CrossRef](#)]
65. Ramoelo, A.; Majazi, N.; Mathieu, R.; Jovanovic, N.; Nickless, A.; Dziki, S. Validation of Global Evapotranspiration Product (MOD16) using Flux Tower Data in the African Savanna, South Africa. *Remote Sens.* **2014**, *6*, 7406–7423. [[CrossRef](#)]

Disclaimer/Publisher’s Note: The statements, opinions and data contained in all publications are solely those of the individual author(s) and contributor(s) and not of MDPI and/or the editor(s). MDPI and/or the editor(s) disclaim responsibility for any injury to people or property resulting from any ideas, methods, instructions or products referred to in the content.